The Journal of Chemical Physics

RESEARCH ARTICLE | OCTOBER 03 2023

Out-of-contact peeling caused by elastohydrodynamic deformation during viscous adhesion

Special Collection: Adhesion and Friction

Xingchen Shao ; Yumo Wang ; Joelle Frechette

Check for updates

J. Chem. Phys. 159, 134904 (2023)
https://doi.org/10.1063/5.0167300
CHORUS

View Online
Export Citation

Articles You May Be Interested In

Effects of distribution density and location of subsurface particles on elastohydrodynamic lubrication

AIP Advances (May 2020)

Elastohydrodynamic lubrication in point contact on the surfaces of particle-reinforced composite

AIP Advances (April 2018)

The elastohydrodynamic force on a sphere near a soft wall

Physics of Fluids (October 2007)

11 August 2025 21:13:12

Webinar From Noise to Knowledge
May 13th – Register now
Zurich Instruments
Universität Konstanz

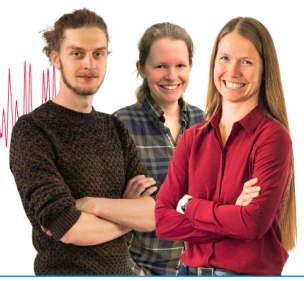

AIP Publishing

The Journal of Chemical Physics ARTICLE pubs.aip.org/aip/jcp

Out-of-contact peeling caused by elastohydrodynamic deformation during viscous adhesion

Cite as: J. Chem. Phys. 159, 134904 (2023); doi: 10.1063/5.0167300
Submitted: 11 July 2023 • Accepted: 12 September 2023 •
Published Online: 3 October 2023

View Online Export Citation CrossMark

Xingchen Shao,[1] Yumo Wang,[2] and Joelle Frechette[1,a)]

AFFILIATIONS

[1] Chemical and Biomolecular Engineering Department, University of California, Berkeley, California 94720, USA
[2] National Engineering Laboratory for Pipeline Safety, Beijing Key Laboratory of Urban Oil and Gas Distribution Technology, China University of Petroleum, Beijing, 18# Fuxue Road, Changping District, 102249 Beijing, China

Note: This paper is part of the JCP Special Topic on Adhesion and Friction.
[a)] **Author to whom correspondence should be addressed:** jfrechette@berkeley.edu

ABSTRACT

We report on viscous adhesion measurements conducted in sphere-plane geometry between a rigid sphere and soft surfaces submerged in silicone oils. Increasing the surface compliance leads to a decrease in the adhesive strength due to elastohydrodynamic deformation of the soft surface during debonding. The force-displacement and fluid film thickness-time data are compared to an elastohydrodynamic model that incorporates the force measuring spring and finds good agreement between the model and data. We calculate the pressure distribution in the fluid and find that, in contrast to debonding from rigid surfaces, the pressure drop is non-monotonic and includes the presence of stagnation points within the fluid film when a soft surface is present. In addition, viscous adhesion in the presence of a soft surface leads to a debonding process that occurs via a peeling front (located at a stagnation point), even in the absence of solid–solid contact. As a result of mass conservation, the elastohydrodynamic deformation of the soft surface during detachment leads to surfaces that come closer as the surfaces are separated. During detachment, there is a region with fluid drainage between the centerpoint and the stagnation point, while there is fluid infusion further out. Understanding and harnessing the coupling between lubrication pressure, elasticity, and surface interactions provides material design strategies for applications such as adhesives, coatings, microsensors, and biomaterials.

Published under an exclusive license by AIP Publishing. https://doi.org/10.1063/5.0167300

11 August 2025 21:13:12

INTRODUCTION

Detachment of surfaces separated by a thin fluid film leads to adhesion because of resistance to fluid infusion.[1,2] Animals such as the frog or chameleon rely on viscous adhesion for prey capture or for locomotion on wet surfaces,[3–6] and bio-inspired soft microstructures leverage this resistance to fluid infusion to control adhesion.[7,8] On the other hand, the same forces can be detrimental and lead to fractures in additive manufacturing processes.[9,10] In these examples, fluid infusion occurs in a narrow gap bounded by soft solids. The lubrication forces associated with the increase in the fluid gap cause elastic deformation that alters the fluid flow and modulates the adhesive strength. The coupling between the local elastic deformation and fluid infusion determines the adhesive force. In particular, surface deformation limits fluid infusion and slows down the detachment process. Despite its importance in multiple naturally occurring and industrial processes, the relationship between fluid flow and elasticity remains poorly understood, especially in regard to their relationship to adhesive strength.

Studies of the adhesive forces during fluid infusion past deformable surfaces are limited. In contrast, the repulsive forces caused by fluid drainage as soft surfaces approach another solid surface (and sometimes make contact) have been investigated more thoroughly.[11–18] Similarly, the forces and deformation associated with small displacements are well-understood and are employed for out-of-contact rheological measurements.[19–23] We previously studied the onset of a peeling process in a viscous fluid and high-

Published under an exclusive license by AIP Publishing

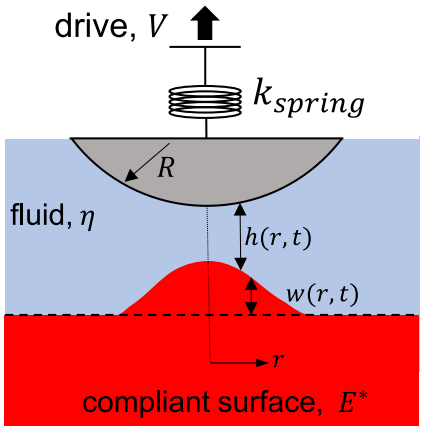

FIG. 1. Schematic of the experimental configuration employed in the experiments and model. The schematic depicts surface deformation, $w(r,t)$, as the surface is separated from an initial separation at the center point ($r = 0$) of h_0.

lighted the coupling between compliance and fluid infusion during it.[24] Here, we narrow our investigation to the sphere–sphere or sphere-plane configuration for its well-defined gap and experimentally accessible geometry (see Fig. 1). In particular, there is a need to predict the peak force (also known as the adhesive strength) and how it depends on material properties (compliance and viscosity) and experimental conditions (velocity and fluid film thickness). Previously, Francis and Horn analyzed the adhesive force caused by the infusion of a viscous fluid between rigid surfaces through experiments and modeling.[25] They obtained an empirical relationship for the adhesive strength, with the first order term being a linear dependence between the peak force and the square root of the system compliance. As a result, they showed that adhesive strength is not a material property but is instead interwoven with system compliance. The validity of the relationship derived by Francis and Horn for elastohydrodynamic adhesion remains to be investigated. More recently, Kaveh and co-workers studied and modeled both approach and retraction forces during infusion past a deformable surface, showing that the presence of a soft surface had profound effects on the adhesive strength.[14] Later, Venketeswaran and Das developed a model for the detachment force during the separation of soft surfaces in the context of 3D printing.[9] Their analysis was extended to weakly compressible materials and conforming surface profiles. Their model described the pressure and deformation profiles during detachment for a broad range of parameters. All these investigations show that the presence of soft surfaces has a profound impact on viscous adhesion, but how elasticity affects viscous adhesion has yet to be elucidated. Beyond the prediction of the adhesive strength, the evolution of the elastic deformation and the pressure drop during detachment remain to be investigated.

In this work, we study the detachment between a soft elastomer and a rigid surface immersed in a viscous fluid (Fig. 1). We directly measure the spatiotemporal fluid film thickness as well as the detachment forces. Throughout, the experimental data are compared to a full model that includes elastohydrodynamic (EHD) deformations and the force measuring spring. We evaluate the role of surface compliance in the adhesive strength and compare it with existing relationships for rigid surfaces. We observe that elastic deformation of the soft surfaces leads to a decrease in adhesive strength and longer detachment times (compared to their rigid counterparts), in agreement with model predictions. We compare the adhesive strength to that predicted for rigid surfaces with comparable compliance to highlight the unique contribution of local surface deformation to adhesion. We also characterize the evolution of the fluid film thickness during detachment and observe that EHD deformations counterintuitively bring surfaces closer during detachment. Our model allows us to monitor the pressure drop and fluid velocity profile during detachment. We see that the pressure drop is non-monotonic, leading to the presence of stagnation points within the fluid film. Finally, we demonstrate that debonding in the presence of a soft surface occurs via a peeling front, similar to the mechanics of adhesive contact. Here, however, the peeling front is located at the stagnation point. A better understanding of viscous adhesion between soft surfaces could have important implications in areas such as haptics,[26] texture perception,[27–29] tribology,[30] or fracture in additive manufacturing.[10]

Elastohydrodynamic adhesion model

To describe the detachment forces and elastic deformation, we adapted a model described and validated in our prior work.[11,31] We consider the detachment in sphere-plane geometry where a fluid is present between the surfaces. The fluid is assumed to be Newtonian, and the central film thickness is at least two orders of magnitude smaller than the radius of the sphere, $h(r = 0, t) \ll R$, allowing us to use the lubrication approximation. In other words, $h \ll R$ in axisymmetric flow and the radial velocity are much larger than the axial velocity $v_z \ll v_r$, as well as the zero azimuthal velocity v_θ and the low Reynolds number $Re \ll 1$.[32,33] By applying the no-slip boundary condition, the flow obeys the following governing equation relating the pressure distribution, $p(r,t)$, to the spatiotemporal fluid film thickness, $h(r,t)$,

$$\frac{\partial h(r,t)}{\partial t} = \frac{1}{12\eta r}\frac{\partial}{\partial r}\left(rh^3\frac{\partial p(r,t)}{\partial r}\right), \tag{1}$$

where η is the viscosity, t is the time, and r is the radial position. We use linear elasticity theory for stratified materials to describe the deformation profile, $w(r,t)$, of the elastic layer due to the fluid pressure distribution. Here, the tangential stress σ_T is negligible at the solid surface, and the fluid pressure is used as the axisymmetric normal stress boundary. The sticky boundary conditions are assumed at the soft/hard interface. We solve for the deformation distribution of the elastic layer by implementing Hankel transforms in the elastohydrodynamic equations. The surface deformation can be calculated from

$$w(r,t) = \int_0^\infty \frac{2}{E^{*\xi}} X(\xi\delta) Z(\xi) J_0(\xi r) d\xi, \tag{2}$$

where

$$X(\xi\delta) = \frac{\gamma\left(1 - e^{-4\xi\delta}\right) - 4\xi\delta e^{-2\xi\delta}}{\gamma\left(1 + e^{-4\xi\delta}\right) + (\gamma^2 + 1 + 4(\xi\delta)^2)e^{-2\xi\delta}}; \quad \gamma = 3 - 4\nu \tag{3}$$

11 August 2025 21:13:12

Published under an exclusive license by AIP Publishing

and

$$Z(\xi) = \xi \int_0^\infty rp(r,t)J_0(\xi r)dr. \tag{4}$$

Here, the soft coating is described by its thickness δ, its Poisson's ratio v, and its reduced Young's modulus E^*. In Eqs. (2)–(4), $Z(\xi)$ is the modified Hankel transform of the pressure, where $J_0(\xi r)$ is the 0^{th}-order Bessel function of the first kind. As this work focuses on the interaction between a rigid sphere and a thick soft layer, we set the thickness of the soft layer as R and the sphere radius to fall within the limit of elastic half space.

In our model, one of the surfaces is mounted on a force-measuring spring. The spring force, F_s, is balanced by the hydrodynamic force as

$$F_s = \int_0^R p(r,t)2\pi r dr = -k_{spring}\Delta x = k_{spring}[h_0 - h(0,t) + Vt + w(0,t)], \tag{5}$$

where k_{spring} is the spring constant of the cantilever, Δx is the spring deflection (negative for attraction), and h_0 is the initial separation at the centerpoint (see Fig. 1). To describe retraction, the sign of the drive velocity V in Eq. (5) is positive (with the convention here that attractive forces are positive), and the deformation is negative (tension). To obtain the spatiotemporal information of all the parameters in this elastohydrodynamic problem, we solve Eqs. (1)–(5) numerically by discretizing time and lateral positions, and the values from the prior time step are used as the first value of the next step. The lateral position in the calculations is always within 10% of R to remain within the lubrication approximation. The lateral domain ($r < 0.1R$) is discretized into 500 evenly spaced elements. For $0.1R < r < R$, the deformation is small enough, i.e., $w(r,t) \ll s(t)$, to be negligible in the pressure calculation, where s is the distance between undeformed surfaces at the centerpoint, $s(t) = h(r,t) - w(r,t)$.[34] In this limit, an asymptotic pressure profile given by

$$p(r,t) = \frac{3\eta RV}{\left(s(t) + r^2/2R\right)^2} \tag{6}$$

is employed for the outer region ($0.1R < r < R$). Using Eq. (6), we obtain values of $p(r,t)$ at $r = 0.1R$, which we use as the pressure boundary for Eq. (1) to solve pressure distribution over the region where $r < 0.1R$. The calculated pressure distribution is the stress boundary of the viscous fluid for the surface deformation calculation within the region $r < 0.1R$. Because of the continuity of the material, the radial deformation profile is larger than the pressure distribution (the pressure decays faster away from the centerpoint than the deformation).

At the first step of our numerical calculation, we estimate the film thickness h_{guess} without considering surface deformation in the initial estimate. The calculated film thickness h_{calc} is obtained by solving Eqs. (1)–(6). In the second iteration step, we update the new estimated film thickness as $h_{guess}{}^* ratio + h_{calc}{}^* (1 - ratio)$, where the *ratio* is introduced to either accelerate or deaccelerate the calculation speed. In the beginning, when the film is at its thinnest, the fluid pressure is very sensitive to small changes in the fluid film thickness. Hence, a conservative ratio value of 0.995 is chosen for each film thickness iteration step to ensure convergence. The ratio automatically decreases by 0.001 for each of the 300 steps if the difference between h_{guess} and h_{calc} is less than 5 nm and no negative film thickness is obtained in all the steps. We run the convergence tests on both r and t until the maximum error of the fluid film thickness h is less than 0.1 nm for all values of r.

The velocity of the fluid between the surfaces is calculated through its relationship with the pressure profile through the incompressible Navier–Stokes equation, given by

$$-\nabla p + \eta\nabla^2 \boldsymbol{v} = 0. \tag{7}$$

We again rely on the lubrication approximation, which Eq. (7) reduces to

$$-\frac{\partial p}{\partial r} + \eta\frac{\partial^2 v_r}{\partial z^2} = 0, \tag{8}$$

$$\frac{\partial p}{\partial z} = 0. \tag{9}$$

We then apply the no slip boundary conditions at the bottom plane $v_{r(z=0)} = 0$, and at the surface of the probe, $v_{r(z=h(r,t))} = 0$, to obtain the velocity field,

$$v_r = \frac{1}{2\eta}\frac{dp}{dr}\left(z^2 - hz\right). \tag{10}$$

The radial pressure gradient $\frac{dp}{dr}$ is calculated from the pressure profile $p(r,t)$ using our EHD model. By solving Eq. (10), we obtain the radial velocity profile of the thin fluid film during detachment. We also rechecked that we remained within the lubrication limit. Using $Re = \frac{\rho UL}{\eta}$, where U is the characteristic velocity (we use the motor velocity, V) and L is the characteristic length (radius of the probe, R). We obtain $Re = 4.5 \times 10^{-5}$ to 1.3×10^{-4}, supporting the low Reynolds number assumption.

We also verify that we remain within the linear elasticity limit for all the experimental conditions investigated here. To do so, we consider the spherical indentation strain, ε, for the sphere-plane geometry based on Hertz's theory as $\varepsilon = \frac{w_0}{\frac{3\pi}{4}a}$, where w_0 is the elastic deformation at the center and a is the effective contact radius defined as $a = \sqrt{w_0 R}$.[35] By using the maximum central deformation as the indentation depth $w_0 = 15\ \mu$m, we obtain a maximum strain of $\varepsilon = 0.0195$, confirming that we remain within the linear elasticity limit. This maximum indentation depth occurs in the experiment where $E = 0.07$ MPa, $\eta = 0.53$ Pa · s, $V = 10\ \mu$m/s, and $h_0 = 500$ nm.

As a final check, we verify the validity of the approximation of negligible shear stress at the solid–liquid interface. To do so, we consider the ratio of the tangential stress to normal stress as $\sigma_T/\sigma_N \sim \sqrt{h_0/R}$.[36] In our experiments, the most extreme case gives $\sqrt{h_0/R} = 0.075$ ($R = 7.1$ mm, $h_{\max} = 40\ \mu$m), confirming that σ_N dominates over σ_T in our experiments. Moreover, in the limit of an elastic half-space, we also expect that the shear stress will be negligible because the hydrodynamic radius is much smaller than the thickness of the soft film.[37] This result allows us to neglect shear stress in the boundary condition. Thus, we only consider the elastic response to the normal pressure acting on the surface.

11 August 2025 21:13:12

Published under an exclusive license by AIP Publishing

MATERIALS AND METHODS

Materials

Experiments in the MFM (Multimode Force Microscope) are conducted with two different silicone oils (Gelest DMS-T22 200 cSt and DMS-H25 500 cST) with viscosities at 25 °C of $\eta = 0.194$ Pa · s and $\eta = 0.485$ Pa · s, respectively. Experiments in the SFA are conducted with $\eta = 0.194$ Pa · s silicone oils (Xiameter PMX 200 Dow Corning). Dow Corning Sylgard 184 elastomer kit is used for the polydimethyl siloxane (PDMS) elastomers for both MFM and SFA experiments. In the MFM, the upper surface is a glass plano-convex lens (R = 7.1 mm). A microscope slide (46 × 27 × 1.2 mm^3) is used as a supporting substrate for the PDMS layer. The roughness of our microscope slides and optical lenses is within 5 nm. The materials for the SFA experiments have been detailed previously.[11] In summary, one surface is a layer of known thickness of the negative photoresist SU-8 (SU-8 2007, MicroChem) as a coating on a muscovite mica sheet (Ruby, ASTM V-1/2, S & J Trading, Glenn Oaks, NY) to serve as a smooth and rigid surface. Silver films are 99.999% pure (Alfa Aesar), and the PDMS is also Sylgard 184.

Sample preparation

(a) MFM experiments To change the elastic modulus of the PDMS, we use ratios of the pre-polymer and crosslinker by weight of 10:1 and 40:1. The two-component mixture is mixed and then stirred for 10 min, followed by a degassing step in vacuum for 20 min. The mixture is then poured into a clean dish to reach a height of 1.5 mm. The thickness of 1.5 mm is significantly larger than the deformation and the hydrodynamic radius, so we can treat the PDMS as a half space. We then cure the PDMS mixture in an oven at 75 °C for 16 h. After the curing, the PDMS sample is carefully cut into a circular shape with a radius equal to 12 mm and placed onto the surface of a glass slide. We did not extract the PDMS to remove unreacted oligomers; we expect that the 10:1 PDMS contains 4 wt % of unreacted oligomers, while the 40:1 contains as much as 40 wt %. The adhesion between the PDMS and the slide is sufficient to anchor the PDMS in space throughout our experiments. The microscope slides and the glass lens are washed in chloroform and rinsed with isopropyl alcohol, then cleaned by immersion in piranha solution (1:3 = H_2O_2/H_2SO_4) for 1 h. (b) SFA experiments We follow the same protocol as Wang and Frechette.[11] In summary, we use PDMS with a 10:1 polymer to crosslinker ratio, extract unreacted oligomers, and plasma treat them and coat them with a 50 nm silver layer. The thickness of the PDMS is 330 μm. The PDMS films are glued to a cylindrical disk.

Rheological measurements

We measure the complex modulus $G = G' + iG''$ of the two PDMS samples with a height of 1.5 mm. A frequency sweep is performed on each sample by using an Anton Paar rheometer (MCR 302); see the supplementary material, Fig. S1 for the rheological data. The loss modulus is one order of magnitude smaller than the storage modulus, and our PDMS sample behaves as linear elastic solids characterized by $G \equiv G'$ in the low frequency region ($\omega < 10$ rad/s). The corresponding Young's modulus for the two ratios 10:1 and 40:1 is $E = 2.1$ and 0.07 MPa, respectively.

MFM measurements

The force during detachment between the elastomer and the glass probe is measured with a custom-built multifunctional force microscope (MFM).[38] A cantilever spring ($k_{spring} = 1021.0$ N/m) is mounted on a micro-translation stage (M112.1 DG, Physik Instrumente). The cantilever deflection is measured through a fiber optic sensor (muDMS-D63, Philtek, Inc.). A glass probe (R = 7.1 mm) is mounted at the end of the cantilever. The drive velocities for the micro-translation stage are set at either $V = 3.5\frac{\mu m}{s}$ *or* 10 μm/s. The glass slide with the PDMS sample is mounted on the MFM and held in place by screwing a rectangular bath on top of the slide. An oil drop of 100 μl is placed between the surfaces prior to force measurements. The elapsed time between oil exposure and the beginning of the experiments is ~20 min. A code written in Labview is used to record the fiber optic sensor and micro-translation stage position data, from which the force as a function of the micro-translation stage position data is recorded. To detect the position of the surface (contact position), we lower the micro-translation stage to its lowest drive velocity, $V = -0.1$ μm/s, to minimize any possible contribution from viscous forces. When we detect an abrupt deflection of the cantilever, we record this position as system z_0, i.e., the drive position when the probe and PDMS first make contact. The microtranslation stage is then pulled up by 200 nm at $V = 0.1$ μm/s and allowed to relax for 20 min. Then the retraction experiment with the prescribed velocity is performed. For the same Young's modulus and viscosity, we repeat the same protocols but by pulling up the micro-translation stage by 500 nm higher than the last run to get the relation of adhesion force with different initial separations. To vary the initial separation, we repeat the same protocol for detecting the contact position but pull up the micro-translation stage by 2000 nm from the contact position. The total time for the experiments (obtaining the force vs time data for different initial separations) is ~2 h. To minimize the swelling of the PDMS due to its absorption of silicone oil, we use a fresh sample in each set of force measurements, and the PDMS sample and oil are replaced for each experiment. Swelling in the experiments appeared limited; we compared the system z_0 (the drive position when the probe and PDMS first make contact) between the beginning and end of our experiments, and the differences are all within 10 nm after ~2 h. Limited swelling for 200 cSt and 500 cSt silicone oils in PDMS is in agreement with the literature precedent.[39] In addition, theoretical work has shown that oil transport within the elastomer matrix should have a limited impact on the elastohydrodynamic response.[22] We note that the motor has some backlash for the microtranslation stage, making it difficult to precisely set the initial separation. Therefore, instead of using the prescribed pulling up distance as the initial separation, we fit the force to obtain the initial separation. The oil viscosity extracted from force vs time over long periods of time is used to account for minute fluctuations in viscosity due to small temperature changes.

SFA measurements

We use the Surface Forces Apparatus (SFA) to measure the spatiotemporal fluid film thickness in the gap between two separate

11 August 2025 21:13:12

Published under an exclusive license by AIP Publishing

surfaces.[11] The experimental protocol has been described previously and summarized here for clarity.[11,13] The experiments are conducted in the cross-cylinder configuration, which is geometrically equivalent to a sphere-plane geometry with a radius of 1.31 cm. The fluid film thickness is measured between a deformable PDMS film with Young's modulus E = 1.05 MPa and Poisson's ratio ~0.5 and a rigid SU-8 surface. The SU-8 surface is mounted on a cantilever spring (k_{spring} = 165 N/m) connected to a stepper motor driving the surfaces apart. The surfaces are fully immersed in silicone oil. The surface separation $h(r,t)$ is measured using white light interferometry between two thin silver layers (50 nm), one of which is evaporated on top of the PDMS film to capture full surface deformation. The contact position (zero separation) is first determined through a quasi-static experiment in the absence of viscous forces. The surfaces are slowly pushed together until a large, flat central contact region forms. For retraction experiments, the interacting surfaces are moved together quasi-statically until they are in a close-to-contact position (tens of nm). The system is then placed at rest for 3 min, followed by retraction at a constant drive velocity of V = 61 nm/s with the motor connected to the lower rigid surface. The spatiotemporal fluid film thickness is then recorded from the interferometric fringes, while the interacting force is recorded by spring deflection.

IV. RESULTS AND DISCUSSION

A. Experimental results for viscous adhesion measurements

We measure the force as a function of time during the detachment of a glass sphere from a PDMS slab for different combinations of experimental parameters (initial separation, viscosity, velocity, and Young's modulus). The representative data is shown in Fig. 2(a) and validates the viscous adhesion model detailed previously. The data follow expected trends: the peak force increases with an increase in velocity and viscosity, and over a long time, the forces collapse into a single curve [inset in Fig. 2(a)] for the motion at a constant velocity, $F = 6\pi R^2 \eta t^{-1}$.[40] We extract the viscosity from the long time limit and find that the values are in close agreement with those reported for the oils (see the supplementary material, Table S1). In addition, in a short time, there is a linear relationship between the force and motor displacement, with the range of the linear regime decreasing when the forces are lower. This linear portion corresponds to a regime of constant compliance with an effective stiffness k_{eff}, where the slope can be interpreted as coming from the deflection of springs in series: $k_{eff}^{-1} = k_{spring}^{-1} + k_{surface}^{-1}$, where k_{spring} is the cantilever spring constant and $k_{surface}$ represents the effective stiffness of the surface (see the supplementary material, Table S1 for values). Between these short- and long-time limits, elasticity and viscous forces are highly coupled, and we are interested in gaining a better understanding of the detachment process between these two limits.

In addition, shown in Fig. 2(a), are the predictions from our viscous adhesion elastohydrodynamic model. We use the initial separation at the centerpoint, h_o, as a fitting parameter for the model and obtain excellent agreement with the experimental data. As expected, we see that for a given set of parameters (E, η, V), the maximum force increases with a decrease in initial separation. We also see

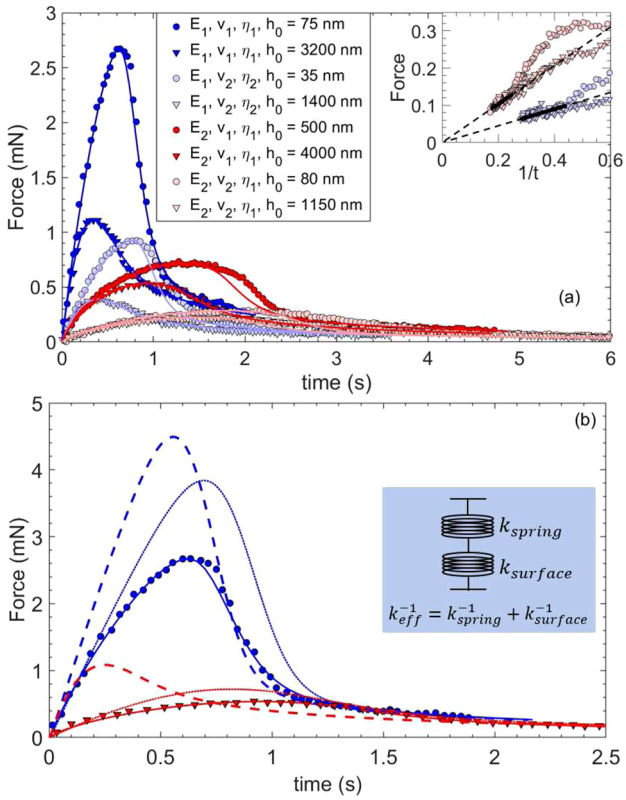

FIG. 2. (a) Force curves from MFM and comparison with predictions from the model with Young modulus E_1 = 2.1 MPa (blue) and E_2 = 0.07 MPa (red), silicone oil with viscosity η_1 = 0.49 Pa · s and η_2 = 0.20 Pa · s, and drive velocity V_1 = 10 μm/s and V_2 = 3.5 μm/s. The inset shows the force vs t^{-1} approaching $F = 6R^2\pi\eta t^{-1}$, indicating the expected linear regime over a long time. The linear fit of the last 20 data points to $F = 6R^2\pi\eta\frac{1}{t}$ is used as a fitting parameter for the viscosity, with η_{f1} = 0.53 Pa · s and η_{f2} = 0.22 Pa · s. (b) Importance of a full model when comparing force curves. The data are compared with a full model (solid line), a rigid limit with an effective spring constant (dotted line), and rigid surfaces where the only compliance is that of the spring. (blue) E = 2.1 MPa, V = 10 μm/s, η_f = 0.53 Pa · s, h_0 = 35 nm, and (red) E = 0.07 MPa, V = 3.5 μm/s, η_f = 0.53 Pa · s, h_0 = 4000 nm. Inset: illustration of the effective spring constant based on the compliance of the surface and the cantilever spring.

that the force curves are greatly affected by surface compliance. For the exact same velocity and viscosity (and relatively similar initial separation), decreasing the elastic modulus of the PDMS slab leads to different retraction curves (see the supplementary material, Fig. S2). We also observe deviations between the model and experimental data near the peak force for the softest surface at the lowest initial separations. These deviations are caused by an elastic (spring instability) occurring when the gradient of the force (dF/ds) is greater than the spring constant, leading the surfaces to "jump" apart.[41] We can determine that the deviations are caused by spring instability from a comparison between the onset of the deviation of the elastohydrodynamic model with the data and the predictions of the spring instability based on the initial compliance and stability criteria (see the supplementary material, Fig. S3).

11 August 2025 21:13:12

Published under an exclusive license by AIP Publishing

An important finding when comparing the experimental data to our model is the need to incorporate the full detail of the surface deformation to capture the detachment curve. Shown in Fig. 2(b) are comparisons of our model with simplified approximations: (i) rigid sphere/plane where the only compliance arises from the cantilever ($k_{eff} = k_{spring}$) and (ii) rigid sphere/plane where we use the measured k_{eff}^{-1} from the initial constant compliance regime as the system's compliance [see inset in Fig. 2(b)] is ignored. We see that completely ignoring elasticity leads to poor agreement with the experimental data (compare the dashed lines with the experimental data). Modeling the system as springs in series (soft surface and cantilever) through effective compliance but ignoring details of the surface deformation profile allows us to capture the initial slope in the force-time curve but largely overestimate the maximum force. Moreover, this approximation leads to poor agreement in the transition region between the elasticity-dominated and hydrodynamic-dominated regimes (compare the dotted lines with the experimental data).

The decrease in the detachment force in the presence of soft surfaces, as shown from the comparison between data points and the dashed lines in Fig. 2(b), is because more energy input from the motor is converted into stored elastic energy rather than fluid viscous dissipation. This decrease in force is captured qualitatively in the effective compliance model, but there are significant disagreements when predicting the temporal evolution of the force unless the full spatiotemporal deformation profile is incorporated. The error in the peak force seems larger in absolute value when comparing the data and the approximate model for the stiffer PDMS. In fact, the relative difference between the experiment and the data is almost the same for the two Young's moduli investigated [Fig. 2(b)]. For the stiffer PDMS, while the overall system compliance is less affected by the presence of the soft surface the local surface, deformation profile still has an important impact on the forces measured, explaining the larger absolute error between the approximate model and the data when compared to the softer PDMS.

Finally, we compare the apparent surface stiffness ($k_{surface}$), obtained from the initial slope of the force-time curves to the values predicted by either the Hertz equation ($k_{surface} = k_{Hertz} = 4/3E^*(Rh_0)^{1/2}$), or by assuming a uniform pressure distribution ($k_{surface} = k_{uni} \sim \pi E^*(Rh_0)^{1/2}$); see the supplementary material, Table S1. We see that neither model is in good agreement with the experimental data, although in most cases they are within an order of magnitude. In all cases, assuming a Hertzian stiffness or a uniform pressure always underestimates the initial slope in the detachment experiments (see the supplementary material, Table S1). This difference in effective stiffness indicates that the lateral range of the surface deformation is much greater than the hydrodynamic radius (the stiffness of a sphere increases with the radius of the deformation). Therefore, while the initial linear detachment regime is governed by the system compliance, the surface compliance cannot be predicted *a priori* from the material properties and initial separation. In the following sections, we will investigate further the local deformation profile and its impact on the forces.

We conducted separate detachment experiments in the SFA, where we can rely on multiple beam interferometry to map the spatiotemporal fluid film thickness. The two interacting surfaces here are a PDMS film coated with a thin layer of silver and a SU-8 photoresist. The surfaces are immersed in a silicone oil with the same viscosity as the one employed for the higher viscosity experiments in the MFM. The fluid film thickness profile at two different time points is shown along with the comparison with our model [Fig. 3(a)]. We also report the experimental and modeled time evolution of both the central fluid film thickness and the fluid film thickness at $\frac{r}{R} = 0.01$, Fig. 3(b). Throughout, we see good agreement between the model and the experiments without the need to use any adjustable parameters. Small deviations between the experiments and the model are likely due to surface roughness/defect.[11]

A feature observed in the SFA experiments that agrees with the viscous adhesion model is an out-of-contact peeling process during detachment. Looking at the fluid film profile in Fig. 3(a), we see that the centerpoint appears pinned while the fluid film thickness increases in the region away from the center. As a reminder, note here that the two surfaces are not in physical contact. The initial separation at the centerpoint prior to detachment is $h_0 = 35$ nm, yet the detachment process is very similar to the case where soft solid surfaces are in physical adhesive contact and the contact area decreases during normal detachment. The next section discusses the dynamics of the detachment process in more detail.

If we look at the time evolution of the fluid film thickness at the center, we see that for a long time, the fluid film thickness was nearly constant [Fig. 3(b)]. In fact, we observe that the surfaces come *closer* as we pull them apart. Then, slightly after the peak force is reached (the red point), we see that the fluid film thickness starts to increase rapidly. Then, if we look at the fluid infusion between the pink and blue points, we see that the surface center moves faster than the motor velocity. This higher speed is caused by the sudden release of stored elastic energy within the compliant PDMS layer. Note that this release of elastic energy is not a cantilever spring instability. After the blue point, we reach the long-time regime, and the centerpoint and the point at $\frac{r}{R} = 0.01$ are almost parallel because the surfaces are no longer deformed.

Due to its practical significance, the peak force, F_p (or adhesive strength), is an important feature when comparing soft and rigid viscous adhesion. Francis and Horn developed an analytical expression for the adhesive strength as a function of initial separation for viscous adhesion in sphere-plane geometry.[25] They derived a characteristic length scale, β given by

$$\beta = \left[\frac{6\pi\eta R^2 V}{k_{spring}}\right]^{1/2}, \tag{11}$$

which arises from the balance between spring and viscous forces. This characteristic length scale was sufficient to collapse all the adhesive strength vs initial separation data for different fluid viscosities, spring constants, and detachment velocities; see the black line in Fig. 4 for the adhesive strength as a function of initial separation. Interestingly, the peak force depends linearly on $\sqrt{k_{spring}}$, the same as for solid–solid contact in the air (no viscous dissipation).[42] We compare the dependence of the peak force on the initial separation using the same scaling as in Francis and Horn for elasto-hydrodynamic adhesion. We show both our model prediction and our experimental data for detachment from a PDMS surface with $E = 2.1$ MPa and $E = 0.07$ MPa.

11 August 2025 21:13:12

Published under an exclusive license by AIP Publishing

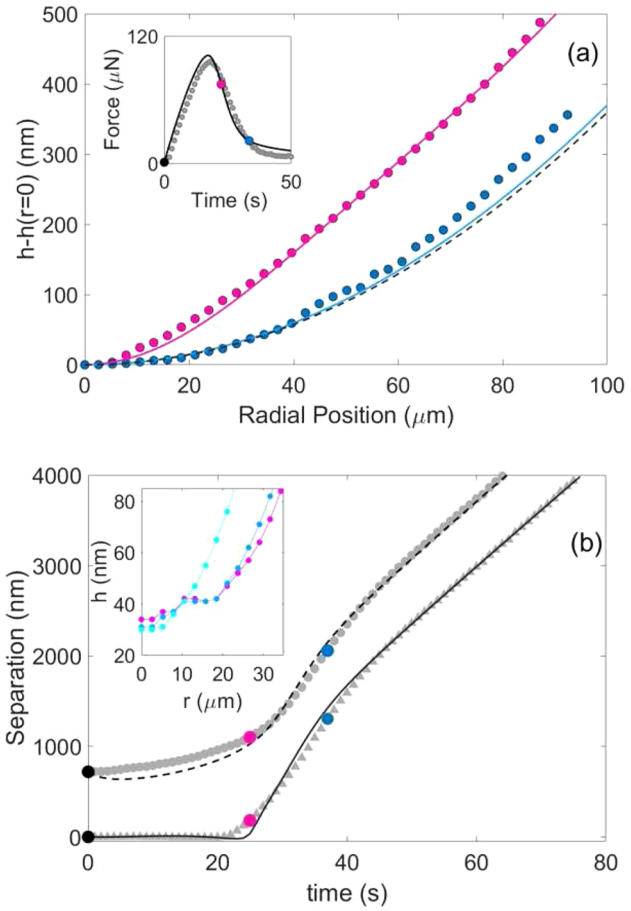

FIG. 3. (a) Direct measurement of fluid film thickness during retraction using the SFA, showing the out-of-contact peeling process. The solid lines represent model prediction without any adjustable parameters but with a shifted hydrodynamic plane of 35 nm due to surface roughness.[11] Experimental conditions are $V = 61\ \mu$m/s, $\eta = 0.194$ Pa · s, $h_0 = 35$ nm, $E = 1.05$ MPa, and $R = 13.1$ mm. The black dashed lines represent the initial film thickness profile. Inset: force vs time data during the retraction process, along with model prediction. Colored data points represent data taken at the same time. The pink points and lines were taken at the time of the largest central deformation. (b) Experiments and model prediction for the temporal film thickness at the centerpoint (triangles, solid line) and at $\frac{r}{R} = 0.01$ (circles, dash line). The colored points serve as indicators for the force curve shown in the inset in (a), and the inset shows the surface profile at $t = 0$ s (purple), $t = 4$ s (dark blue), and $t = 10$ s (light blue), showing the surfaces approaching during retraction.

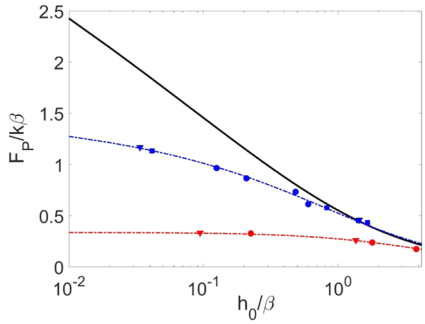

FIG. 4. Model predictions of the peak force (F_p) against scaled initial separation for the detachment from an elastic substrate with E = 2.1 MPa (dashed blue line) and E = 0.07 MPa (dashed red line), respectively, at V = 3.5, 7, and 10 $\frac{\mu m}{s}$ and fluid viscosity $\eta = 2.2$, and 5.3 Pa · s. The characteristic length $\beta = [\frac{6\pi\eta R^2 V}{k_{spring}}]^{1/2}$ represents the balance between spring force and viscous force. The cantilever spring constant $k = k_{spring}$ is used in the nondimensionalization. The data collapses on a single curve for the different experimental parameters, but the curves do not collapse for different Young's moduli. The relationship for the viscous adhesion between rigid surfaces (solid black line) is from Horn *et al.*[25] and is used as a benchmark for the case of F_p where no elastic deformation is present. The blue points represent the experimental data for $E = 2.1$ MPa at $V = 3.5\frac{\mu m}{s}$, $\eta = 2.2$ Pa · s(square); $V = 7\frac{\mu m}{s}$, $\eta = 2.2$ Pa · s(circle); $V = 10\frac{\mu m}{s}$, $\eta = 5.3$ Pa · s(triangle). The red points represent the result of E = 0.07 MPa at $V = 3.5\frac{\mu m}{s}$, $\eta = 5.3$ Pa · s(triangle); and $V = 10\frac{\mu m}{s}$, $\eta = 5.3$ Pa · s(circle).

We find that for a given Young modulus, the scaling from Francis and Horn also collapses the data for the viscous adhesion between soft surfaces. The fact that the Francis and Horn scaling works even for detachment between soft surfaces indicates that velocity, spring constant, and viscosity play a similar role in determining the peak force for viscous adhesion between rigid surfaces. However, as we see in Fig. 4, the scaling does not collapse the data for different Young moduli. Replacing the cantilever compliance with the effective compliance by treating the soft surface and cantilever as springs in series also does not lead to a collapse in the data (and this approximation fails at predicting the peak force as shown in Fig. 2).

B. Predicted deformation, pressure, and velocity profiles

The predicted fluid film thickness at four different time points is shown in Figs. 5(a) and 5(b). The time points correspond to key features of the detachment curve, as shown in the inset. The initial fluid film thickness, where the surface is undeformed, is shown as the black dashed line. The fluid film thickness is axisymmetric; therefore, only half is plotted, and the value for the fluid film thickness at the centerpoint has been subtracted to better visualize the evolution of the profile during detachment. We see that the fluid film thickness departs from the initial parabolic profile as the surfaces detach because of surface deformation. Shortly after the peak force, the fluid film thicknesses recover to their initial undeformed profile. We also plot the fluid film thickness as a function of time at the centerpoint and at $r/R = 0.02$ [Figs. 5(c) and 5(d)]. We see that the fluid film thickness remains nearly constant at the center during detachment until the peak force is reached. In fact, the fluid film thickness at the centerpoint *decreases* (the surfaces get closer to each other) as the surfaces are pulled apart; see the inset in Fig. 5(d), for example.

A careful look at Fig. 5(a) along with Fig. 5(c) [or Figs. (5b) and 5(d)] shows that detachment occurs via *peeling* from the outer region, while the centerpoint remains relatively fixed in place. This

11 August 2025 21:13:12

Published under an exclusive license by AIP Publishing

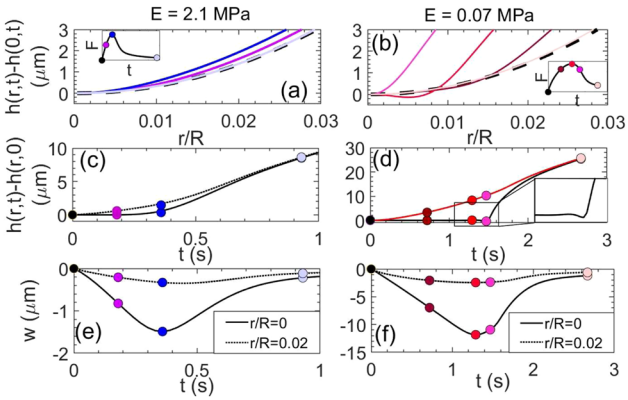

FIG. 5. (a)-(b): Predicted spatiotemporal film thickness profile $h(r,t) - h(0,t)$ with retraction velocity $V = 10\ \mu$m/s, viscosity $\eta = 0.53$ Pa · s, and $h_0 = 900$ nm and (a) E = 2.1 MPa and (b) E = 0.07 MPa. Black dashed lines represent the initial fluid film thickness profile with no deformation. Insets of (a) and (b): lighter colors indicate later times during the retraction process. The insets indicate the corresponding force curve, showing the time points at which the profiles are shown. (c) and (d): Time evolution of the fluid film thickness $h(r,t) - h(r,0)$ at the centerpoint (black solid lines) and at $r/R = 0.02$ (black dotted lines). The points indicate the same times as those in (a) and (b), with lighter colors indicating time progression. (e) and (f): Time evolution of the deformation profile at the center point ($r/R = 0$, solid lines) and $r/R = 0.02$ (dotted lines).

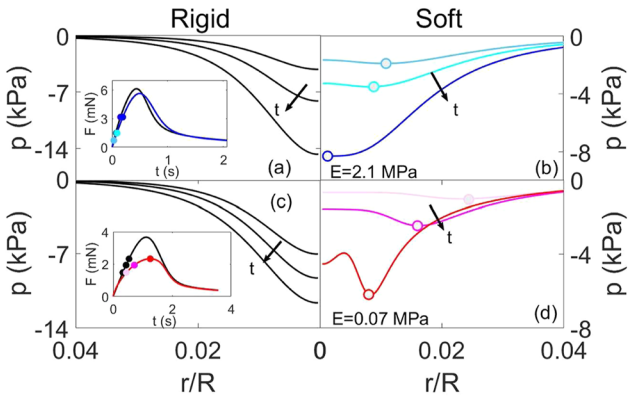

FIG. 6. Role of surface compliance on pressure distribution. Pressure distribution during retraction was calculated at different time points with $V = 10\ \mu$m/s, $\eta = 0.53$ Pa · s, and $h_0 = 900$ nm. (a) rigid surface (black curves) with the same effective stiffness as (b) $E = 2.1$ MPa (blue curves). (c) rigid surface (black curves) with the same effective stiffness as (d) $E = 0.07$ MPa (red curves). The insets of (a) and (c) show the corresponding force curve, where the detachment force for the rigid surface is in black and the soft surface is the colored line. Time progression is indicated with arrows as well as with lighter colored lines. The time points selected are shown in the force curves in the inset. The stagnation points are indicated by the highlighted points in (b) and (c).

out-of-contact peeling is surprising considering that there is no solid–solid contact and that the detachment occurs via the normal motion of the upper surface with respect to the lower one. As a comparison, we plot the fluid film profile during the detachment of two rigid surfaces with the same effective compliance as the rigid–soft pair investigated in our experiments, i.e., the spring stiffness is equal to the k_{eff} from the experiments. In that case, we observe a quick increase in the fluid film thickness with time to allow for fluid infusion (see the supplementary material, Fig. S3). Therefore, the out-of-contact peeling is caused by the compliance of the soft surface.

Local tensile deformation of the soft surface is necessary to maintain a constant (or decreasing) fluid film thickness during detachment (because of volume conservation). We plot the surface deformation at two radial positions: at the centerpoint and also at $r/R = 0.02$ in Figs. 5(e) and 5(f). We see that the surface deformation is greatest at the centerpoint and that further away from the center, the tensile deformation is much smaller. By $\frac{r}{R} \sim 0.03$, the deformation is negligible. Decreasing the elastic modulus from 2.1 to 0.07 MPa alters the detachment process, as shown by comparing the two columns in Fig. 5. First, the features of the deformation profile are comparable, but the extent of surface deformation is much more significant for the softer surface [Figs. 5(e) and 5(f)]. Second, we see that the surface deformation leads to a dimple that forms at the centerpoint for the softer surface, along with detachment occurring via peeling from outside of the centerpoint inward [Fig. 5(b)]. The dimple is absent in the more rigid PDMS. The presence of a dimple in the softest PDMS is surprising, as dimples typically occur because of fluid drainage during normal approach.[13] Here, the dimple appears during normal retraction, where fluid infusion is expected. Finally, we observe that the fluid film thickness at the centerpoint remains nearly constant (or decreases) for a significantly longer period when the modulus of the surface decreases [Figs. 5(c) and 5(d)].

The pressure distribution within the fluid during detachment provides insights into the fluid infusion process and associated detachment forces. We calculate the pressure distribution at different time points during detachment for two compliant surfaces ($E = 2.1$ MPa and $E = 0.07$ MPa); see Fig. 6. For comparison, we also calculate the pressure distribution during the detachment of rigid surfaces with cantilever spring stiffnesses adjusted to match the effective compliance measured in the detachment of the soft surfaces, i.e., the initial slope in the force-time curve is identical; see insets in Figs. 6(a) and 6(c). For the two rigid cases, changing the spring compliance does not lead to qualitative differences in the pressure distribution [Figs. 6(a) and 6(c)]. In both cases, the profile is monotonic or parabolic, and both the range and magnitude of the pressure drop are comparable.

Introducing a soft surface leads to significant differences in pressure distribution. First, the range of the pressure drop is larger when one of the surfaces is deformable, but the magnitude of the pressure is significantly lower. Note here that the detachment force for the selected timepoint is comparable, yet the pressure distribution is very different. Importantly, the radial pressure drop is no longer monotonic when a surface is soft. At each time, there is a radial location where the gradient of the pressure is at a minimum, indicative of a stagnation point within the gap [the stagnation points are shown in Figs. 6(b) and 6(d)]. In contrast to the detachment between rigid surfaces, the stagnation point is not located at the centerpoint. The presence of these stagnation points is due to local elastic surface deformation. In contrast, a monotonic pressure drop is always observed on a rigid surface, and the maximum pressure is

11 August 2025 21:13:12

Published under an exclusive license by AIP Publishing

reached at the center ($r = 0$). During the detachment between a soft and a rigid surface, the direction of the flow reverses at the stagnation point. Therefore, during detachment, there is fluid infusion when $r > r|_{\frac{dp}{dr}=0}$ and drainage when $r < r|_{\frac{dp}{dr}=0}$. When $E = 2.1$ MPa, drainage leads to tensile deformation in the gap, keeping the surface separation at the centerpoint nearly constant (or even bringing the surfaces closer). However, when the compliance of the surface decreases further, the pressure caused by fluid drainage leads to the formation of a blister at the center (but deformation remains tensile), making these dimples different from those observed during drainage[13] but analogous to those observed during particle rebound.[43]

To better reveal the relationship between the fluid pressure and elastic deformation during retraction, we plot the radial velocity field contour of the fluid film in temporal sequence for the two compliant surfaces investigated: $E = 2.1$ MPa [Figs. 7(a)–7(d)] and $E = 0.07$ MPa [Figs. 7(e) and 7(h)]. The magnitude and direction of the velocity vector are shown through the color bar. The initial film thickness is plotted in red dashed lines. The out-of-contact peeling process is visible by comparing the contour of the surface to the red dashed line. Importantly, we see here that the "peeling front" is located at the outer stagnation point and moves inward with the stagnation point during retraction; see the red dots in Fig. 7. We use black arrows in Fig. 7 to illustrate the direction of the fluid in the vicinity of the stagnation points. For the surface with $E = 2.1$ MPa [Figs. 7(b)–7(d)], we see that during retraction, fluid *drainage* occurs from the center up to the stagnation point, and fluid *infusion* is present at radial positions greater than the position of the stagnation point. The constraint of volume conservation forces the fluid film thickness to remain nearly constant in the region where drainage is present during retraction, as shown in Figs. 4(b) and 4(c), as the surfaces detach via peeling at the outer stagnation point. Due to the combination of fluid infusion and drainage, the retraction force coming from fluid infusion is now dissipated farther away from the center. For the surface that is even softer ($E = 0.07$ MPa), Figs. 7(f)–7(h), we see an additional region where a transition from infusion to drainage is present, along with a more complex deformation profile within the region where r is smaller than the position of the outer stagnation point. The second (inner) stagnation point is also located at the undeformed radial position, indicating that additional energy is dissipated through elastic deformation, causing a lower retraction force.

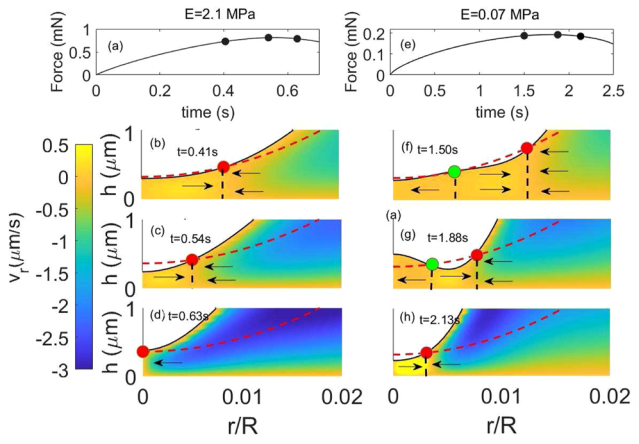

FIG. 7. Velocity field contour in temporal sequence during retraction at $V = 3.5$ μm/s with $\eta = 0.22$ Pa · s, $h_0 = 300$ nm for (a)–(d) $E = 2.10$ MPa with the time points shown in the force curve in (a), and (e)–(h) $E = 0.07$ MPa with the time points shown in the force curve in (e). The red dashed lines represent the initial (undeformed) fluid film thickness $h(r, t = 0)$. The colored points represent the locations of the stagnation points. We observe one stagnation point (red) at E = 2.1 MPa, whereas two stagnation points (red and green) are observed for $E = 0.07$ MPa for t < 2.13 s. The black arrows display the direction of the radial velocity in the vicinity of the pressure stagnation points.

V. CONCLUSIONS

We characterized and modeled the viscous adhesion between a rigid sphere and a soft PDMS surface separated by viscous silicone oils. There was excellent agreement between the experimental data and our model. During detachment, the viscous forces caused elastohydrodynamic deformation of the soft surface. We found that the presence of a soft surface leads to important changes in the detachment force, especially a decrease in the adhesive strength. Modeling of the detachment process showed that elastohydrodynamics has profound effects on the fluid film thickness, elastic deformation, pressure drop, and velocity profile. In particular, we observed the following:

(1) Out-of-contact peeling: Elastohydrodynamic deformation leads to a detachment process that bears many resemblances to peeling, but in the absence of solid–solid contact. Detachment occurs with the outer region moving outward first, while the region near the center essentially remains static (and comes closer to contact).
(2) Stagnation point: Deformation of the soft surface leads to the appearance of a stagnation point in the fluid flow that moves inward (toward the centerpoint) as the surfaces are pulled apart.
(3) Region of drainage and infusion: The presence of the stagnation point implies that both fluid drainage and infusion occur during detachment. Near the centerpoint, there is fluid drainage, while in the outer region, there is fluid infusion.
(4) Surfaces approach during retraction: The tensile deformation of the soft surface leads to a decrease in the fluid film thickness during retraction, which counterintuitively brings the surfaces closer. Experimental data with the surface forces apparatus confirm this model prediction.

These observations indicate that while the adhesive strength decreases when one of the surfaces is soft, the viscous adhesion "bond" can be maintained for a longer period of time because the center separation remains constant as the surface detaches from the outside. The ability to maintain a constant fluid film thickness could have implications for prey prehension or capture where a viscous mucus layer is present (for example, in frogs or chameleons).[3,6] In these cases, the elastohydrodynamic coupling between the tongues and mucus could help keep the prey in place even in the absence of solid–solid contact. Similarly, elastohydrodynamic coupling could help (or hinder) picking and placing soft objects when a fluid is present, such as in soft robotics,[44] sensing,[45] or haptics.[26]

11 August 2025 21:13:12

Published under an exclusive license by AIP Publishing

SUPPLEMENTARY MATERIAL

The supplementary material is available and contains the rheological characterization of the PDMS, a set of experimental parameters, additional force-displacement curves, an analysis of spring instability, and details on force calculations. Matlab code is available at https://github.com/xingchenshao1/Viscous_adhesion_model.

ACKNOWLEDGMENTS

This work was supported by the ACS Petroleum Research Fund (No. 58606-ND5) and the National Science Foundation (No. CMMI 1728082). Y.W. acknowledges support from the National Natural Science Foundation of China (Grant No. 51804319) and the Science Foundation of China University of Petroleum, Beijing (Grant No. 2462018YJRC002).

AUTHOR DECLARATIONS

Conflict of Interest

The authors have no conflicts to disclose.

Author Contributions

Xingchen Shao: Conceptualization (equal); Data curation (equal); Formal analysis (equal); Investigation (equal); Methodology (equal); Visualization (equal); Writing – original draft (equal); Writing – review & editing (equal). **Yumo Wang**: Conceptualization (supporting); Formal analysis (supporting); Investigation (supporting); Methodology (supporting); Writing – original draft (equal); Writing – review & editing (supporting). **Joelle Frechette**: Conceptualization (equal); Funding acquisition (lead); Investigation (equal); Methodology (equal); Project administration (lead); Supervision (lead); Writing – original draft (equal); Writing – review & editing (equal).

DATA AVAILABILITY

The data that support the findings of this study are available from the corresponding author upon reasonable request.

NOMENCLATURE

Variable definition

a	Effective contact radius
E	Young's modulus
E^*	Reduced Young's modulus
F	Force
F_s	Spring force
G	Complex modulus
G'	Storage modulus
G''	Loss modulus
h_0	Initial film thickness at the centerpoint
$h_{\max}$	Maximum film thickness at the centerpoint
$h(r,t)$	Fluid film thickness
h_{guess}	Estimated film thickness in the numerical model prior to convergence
h_{calc}	Calculated film thickness in the numerical model prior to convergence
i	Iota
k_{eff}	Effective stiffness
k_{spring}	Spring constant of the cantilever
$k_{surface}$	Stiffness of the elastic surface
k_{uni}	Stiffness of the surface predicted by uniform pressure distribution
k_{Hertz}	Stiffness of the surface predicted by Hertz equation
p	Pressure
$p(r,t)$	Pressure distribution
r	Radial coordinate
R	Radius of the sphere
$s(t)$	Undeformed separation between the surfaces at the centerpoint
t	Time
$\boldsymbol{v}$	Fluid velocity vector
v_r	Radial fluid velocity
v_z	Axial fluid velocity
v_θ	Azimuthal fluid velocity
V	Drive velocity of the micro-translation stage
w	Elastic layer deformation
w_0	Elastic layer deformation at the centerpoint
$w(r,t)$	Elastic layer deformation expressed as a function of radial position and time
x	Coordinate measured in the direction of the spherical probe
Δx	Spring deflection
z	Axial coordinate
β	Characteristic length defined by Francis and Horn[25]
δ	Thickness of the Elastic layer
ε	Strain
ω	Angular frequency
η	Viscosity
η_f	Fitted viscosity
ν	Poisson's ratio
ρ	Fluid density
σ_N	Normal stress
σ_T	Tangential stress

REFERENCES

[1] Y. Wang, Z. Feng, and J. Frechette, "Dynamic adhesion due to fluid infusion," Curr. Opin. Colloid Interface Sci. **50**, 101397 (2020).

[2] L. Dorogin, A. Tiwari, C. Rotella, P. Mangiagalli, and B. N. J. Persson, "Adhesion between rubber and glass in dry and lubricated condition," J. Chem. Phys. **148**(23), 234702 (2018).

[3] F. Brau, D. Lanterbecq, L.-N. Zghikh, V. Bels, and P. Damman, "Dynamics of prey prehension by chameleons through viscous adhesion," Nat. Phys. **12**(10), 931–935 (2016).

[4] D. M. Drotlef, L. Stepien, M. Kappl, W. J. P. Barnes, H. J. Butt, and A. del Campo, "Insights into the adhesive mechanisms of tree frogs using artificial mimics," Adv. Funct. Mater. **23**(9), 1137–1146 (2013).

[5] J. Iturri, L. Xue, M. Kappl, L. García-Fernández, W. J. P. Barnes, H. J. Butt, and A. del Campo, "Torrent frog-inspired adhesives: Attachment to flooded surfaces," Adv. Funct. Mater. **25**, 1499–1505 (2015).

11 August 2025 21:13:12

Published under an exclusive license by AIP Publishing

[6]A. C. Noel and D. L. Hu, "The tongue as a gripper," J. Exp. Biol. **221**(7), jeb176289 (2018).
[7]Y. Wang, R. Hensel, and E. Arzt, "Attachment of bioinspired microfibrils in fluids: Transition from a hydrodynamic to hydrostatic mechanism," J. R. Soc. Interface **19**(189), 20220050 (2022).
[8]C. Dhong and J. Fréchette, "Coupled effects of applied load and surface structure on the viscous forces during peeling," Soft Matter **11**(10), 1901–1910 (2015).
[9]A. Venketeswaran and S. Das, "Effective and efficient characterization of lubrication flow over soft coatings," Meccanica **55**(6), 1193–1213 (2020).
[10]H. Ye, A. Venketeswaran, S. Das, and C. Zhou, "Investigation of separation force for constrained-surface stereolithography process from mechanics perspective," Rapid Prototyping J. **23**(4), 696–710 (2017).
[11]Y. Wang and J. Frechette, "Morphology of soft and rough contact via fluid drainage," Soft Matter **14**(37), 7605–7614 (2018).
[12]Y. Wang, G. A. Pilkington, C. Dhong, and J. Frechette, "Elastic deformation during dynamic force measurements in viscous fluids," Curr. Opin. Colloid Interface Sci. **27**, 43–49 (2017).
[13]Y. Wang, C. Dhong, and J. Frechette, "Out-of-contact elastohydrodynamic deformation due to lubrication forces," Phys. Rev. Lett. **115**(24), 248302 (2015).
[14]F. Kaveh, J. Ally, M. Kappl, and H.-J. r. Butt, "Hydrodynamic force between a sphere and a soft, elastic surface," Langmuir **30**(39), 11619–11624 (2014).
[15]Z. Liu, H. Dong, A. Jagota, and C.-Y. Hui, "Lubricated soft normal elastic contact of a sphere: A new numerical method and experiment," Soft Matter **18**(6), 1219–1227 (2022).
[16]A. Gopinath and L. Mahadevan, "Elastohydrodynamics of wet bristles, carpets and brushes," Proc. R. Soc. A **467**(2130), 1665–1685 (2011).
[17]V. Bertin, Y. Amarouchene, E. Raphael, and T. Salez, "Soft-lubrication interactions between a rigid sphere and an elastic wall," J. Fluid Mech. **933**, A23 (2022).
[18]M. Sun, N. Kumar, A. Dhinojwala, and H. King, "Attractive forces slow contact formation between deformable bodies underwater," Proc. Natl. Acad. Sci. U. S. A. **118**(41), e2104975118 (2021).
[19]S. Leroy, A. Steinberger, C. Cottin-Bizonne, A. M. Trunfio-Sfarghiu, and E. Charlaix, "Probing biolubrication with a nanoscale flow," Soft Matter **5**(24), 4997–5002 (2009).
[20]S. Leroy, A. Steinberger, C. Cottin-Bizonne, F. Restagno, L. Leger, and E. Charlaix, "Hydrodynamic interaction between a spherical particle and an elastic surface: A gentle probe for soft thin films," Phys. Rev. Lett. **108**(26), 264501 (2012).
[21]R. Villey, E. Martinot, C. Cottin-Bizonne, M. Phaner-Goutorbe, L. Léger, F. Restagno, and E. Charlaix, "Effect of surface elasticity on the rheology of nanometric liquids," Phys. Rev. Lett. **111**(21), 215701 (2013).
[22]C. Kopecz-Muller, V. Bertin, E. Raphael, J. D. McGraw, and T. Salez, "Mechanical response of a thick poroelastic gel in contactless colloidal-probe rheology," Proc. R. Soc. A **479**(2271), 20220832 (2023).
[23]Z. Zhang, M. Arshad, V. Bertin, S. Almohamad, E. Raphaël, T. Salez, and A. Maali, "Contactless rheology of soft gels over a broad frequency range," Phys. Rev. Appl. **17**(6), 064045 (2022).
[24]C. Dhong and J. Fréchette, "Peeling flexible beams in viscous fluids: Rigidity and extensional compliance," J. Appl. Phys. **121**(4), 044906 (2017).
[25]B. Francis and R. G. Horn, "Apparatus-specific analysis of fluid adhesion measurements," J. Appl. Phys. **89**(7), 4167–4174 (2001).
[26]Y. Peng, C. M. Serfass, A. Kawazoe, Y. Shao, K. Gutierrez, C. N. Hill, V. J. Santos, Y. Visell, and L. C. Hsiao, "Elastohydrodynamic friction of robotic and human fingers on soft micropatterned substrates," Nat. Mater. **20**(12), 1707–1711 (2021).
[27]E. Andablo-Reyes, M. Bryant, A. Neville, P. Hyde, R. Sarkar, M. Francis, and A. Sarkar, "3D biomimetic tongue-emulating surfaces for tribological applications," ACS Appl. Mater. Interfaces **12**(44), 49371–49385 (2020).
[28]S. Soltanahmadi, M. Bryant, and A. Sarkar, "Insights into the multiscale lubrication mechanism of edible phase change materials," ACS Appl. Mater. Interfaces **15**(3), 3699–3712 (2023).
[29]C. Dhong, R. Miller, N. B. Root, S. Gupta, L. V. Kayser, C. W. Carpenter, K. J. Loh, V. S. Ramachandran, and D. J. Lipomi, "Role of indentation depth and contact area on human perception of softness for haptic interfaces," Sci. Adv. **5**(8), eaaw8845 (2019).
[30]C. Rotella, B. N. J. Persson, M. Scaraggi, and P. Mangiagalli, "Lubricated sliding friction: Role of interfacial fluid slip and surface roughness," Eur. Phys. J. E **43**(2), 9 (2020).
[31]Y. Wang, M. R. Tan, and J. Frechette, "Elastic deformation of soft coatings due to lubrication forces," Soft Matter **13**(38), 6718–6729 (2017).
[32]L. Wu and D. B. Bogy, "A generalized compressible Reynolds lubrication equation with bounded contact pressure," Phys. Fluids **13**(8), 2237–2244 (2001).
[33]J. B. Shukla, S. Kumar, and P. Chandra, "Generalized Reynolds equation with slip at bearing surfaces: Multiple-layer lubrication theory," Wear **60**(2), 253–268 (1980).
[34]R. H. Davis, J.-M. Serayssol, and E. Hinch, "The elastohydrodynamic collision of two spheres," J. Fluid Mech. **163**, 479–497 (1986).
[35]S. Pathak and S. R. Kalidindi, "Spherical nanoindentation stress–strain curves," Mater. Sci. Eng., R **91**, 1–36 (2015).
[36]S. Leroy and E. Charlaix, "Hydrodynamic interactions for the measurement of thin film elastic properties," J. Fluid Mech. **674**, 389–407 (2011).
[37]J. Li and T.-W. Chou, "Elastic field of a thin-film/substrate system under an axisymmetric loading," Int. J. Solids Struct. **34**(35-36), 4463–4478 (1997).
[38]P. Roberts, G. A. Pilkington, Y. Wang, and J. Frechette, "A multifunctional force microscope for soft matter with in situ imaging," Rev. Sci. Instrum. **89**(4), 043902 (2018).
[39]R. Dangla, F. Gallaire, and C. N. Baroud, "Microchannel deformations due to solvent-induced PDMS swelling," Lab Chip **10**(21), 2972–2978 (2010).
[40]O. I. Vinogradova, H. J. Butt, G. E. Yakubov, and F. Feuillebois, "Dynamic effects on force measurements. I. Viscous drag on the atomic force microscope cantilever," Rev. Sci. Instrum. **72**(5), 2330–2339 (2001).
[41]J. N. Israelachvili, *Intermolecular and Surface Forces: Revised*, 3rd ed. (Academic Press, 2011).
[42]M. D. Bartlett and A. J. Crosby, "Scaling normal adhesion force capacity with a generalized parameter," Langmuir **29**(35), 11022–11027 (2013).
[43]M. R. Tan, Y. Wang, and J. Frechette, "Criterion for particle rebound during wet collisions on elastic coatings," Phys. Rev. Fluids **4**(8), 084305 (2019).
[44]D. Rus and M. T. Tolley, "Design, fabrication and control of soft robots," Nature **521**(7553), 467–475 (2015).
[45]C. Dhong, S. J. Edmunds, J. Ramírez, L. V. Kayser, F. Chen, J. V. Jokerst, and D. J. Lipomi, "Optics-free, non-contact measurements of fluids, bubbles, and particles in microchannels using metallic nano-islands on graphene," Nano Lett. **18**(8), 5306–5311 (2018).

11 August 2025 21:13:12

Published under an exclusive license by AIP Publishing